Radiology

Multiregional Radiogenomic Assessment of Prostate Microenvironments with Multiparametric MR Imaging and DNA Whole-Exome Sequencing of Prostate Glands with Adenocarcinoma[1]

Neema Jamshidi, MD, PhD
Daniel J. Margolis, MD
Steven Raman, MD
Jiaoti Huang, MD, PhD
Robert E. Reiter, MD
Michael D. Kuo, MD

Purpose: To assess the underlying genomic variation of prostate gland microenvironments of patients with prostate adenocarcinoma in the context of colocalized multiparametric magnetic resonance (MR) imaging and histopathologic assessment of normal and abnormal regions by using whole-exome sequencing.

Materials and Methods: Six patients with prostate adenocarcinoma who underwent robotic prostatectomy with whole-mount preservation of the prostate were identified, which enabled spatial mapping between preoperative multiparametric MR imaging and the gland. Four regions of interest were identified within each gland, including regions found to be normal and abnormal via histopathologic analysis. Whole-exome DNA sequencing (>50 times coverage) was performed on each of these spatially targeted regions. Radiogenomic analysis of imaging and mutation data were performed with hierarchical clustering, phylogenetic analysis, and principal component analysis.

Results: Radiogenomic multiparametric MR imaging and whole-exome spatial characterization in six patients with prostate adenocarcinoma (three patients, Gleason score of 3 + 4; and three patients, Gleason score of 4 + 5) was performed across 23 spatially distinct regions. Hierarchical clustering separated histopathologic analysis–proven high-grade lesions from the normal regions, and this reflected concordance between multiparametric MR imaging and resultant histopathologic analysis in all patients. Seventy-seven mutations involving 29 cancer-associated genes across the 23 spatially distinct prostate samples were identified. There was no significant difference in mutation load in cancer-associated genes between regions that were proven to be normal via histopathologic analysis (34 mutations per sample ± 19), mildly suspicious via multiparametric MR imaging (37 mutations per sample ± 21), intermediately suspicious via multiparametric MR imaging (31 mutations per sample ± 15), and high-grade cancer (33 mutations per sample ± 18) (P = .30). Principal component analysis resolved samples from different patients and further classified samples (regardless of histopathologic status) from prostate glands with Gleason score 3 + 4 versus 4 + 5 samples.

Conclusion: Multiregion spatial multiparametric MR imaging and whole-exome radiogenomic analysis of prostate glands with adenocarcinoma shows a continuum of mutations across regions that were found via histologic analysis to be high grade and normal.

Online supplemental material is available for this article.

[1] From the Departments of Radiological Sciences (N.J., S.R., M.D.K.) and Urology (R.E.R.), University of California, Los Angeles–David Geffen School of Medicine, 10833 LeConte Ave, Box 951721, CHS 17-135, Los Angeles, CA 90095-1721; Department of Radiology, Weill Cornell Imaging, New York-Presbyterian Hospital, New York, NY (D.J.M.); Department of Pathology, Duke University School of Medicine, Durham, NC (J.H.); and College of Electrical and Computer Engineering, National Chiao Tung University, HsinChu, Taiwan (M.D.K.). Received December 13, 2016; revision requested January 13, 2017; revision received March 1; accepted March 21; final version accepted April 5. **Address correspondence to** M.D.K. (e-mail: *mikedkuo@gmail.com*).

N.J. supported by the Prostate Cancer Foundation (the Stewart Rahr–PCF Young Investigator Award). M.D.K. and N.J. supported by UCLA Prostate Cancer Spore Career Development Award (NCI SPORE 2P50CA092131).

Prostate cancer is the most prevalent malignancy in men and third most common cause of death because of malignancy (1). The phenotype and course of the disease span a broad spectrum, from an indolent tumor to an aggressive metastatic carcinoma (2,3). Whereas there continue to be advancements in screening and treatment, some of the basic underlying biologic processes regarding gland changes over decades of life have yet to be elucidated.

The recognition and appreciation of neoplasia as an evolutionary process has long been recognized (4–6). As technological capabilities have advanced there has been deeper characterization of tumors by histopathologic analysis, clinical imaging, and high-throughput data analysis that has shed further light on mechanisms of development, progression, and differences in tumor grade and aggressiveness (7,8). Intratumoral heterogeneity has been highlighted as a feature of multiple malignancies (9); however, variation in the imaging appearance, histopathologic analysis, and whole-exome variation within tumors and their surrounding microenvironments proven to be normal via histopathologic analysis have not, to our knowledge, been explored.

In recent years, radiogenomics has become an increasingly popular approach for linking molecular phenotyping with clinical imaging (10–17). Simultaneous characterization of macroscopic multiparametric magnetic resonance (MR) imaging features with microscopic genomic signatures in the context of well-defined histopathologic structure in a spatially colocalized manner may further inform the underlying variation of microenvironments in prostate glands that developed adenocarcinomatous nodules.

We set forth to further evaluate these features simultaneously in prostate glands with confirmed adenocarcinoma by histopathologic analysis (Gleason score, >6). We leveraged the colocalization ability of preserved whole-mount prostates, resected for treatment of adenocarcinoma, with preoperative multiparametric MR imaging to selectively interrogate multiple regions of interest, including regions determined via histopathologic analysis to be abnormal as well as normal by using whole-exome DNA sequencing (sequencing all of the expressed genes in the human genome). The purpose of this study was to assess the underlying genomic variation of prostate gland microenvironments in patients with prostate adenocarcinoma in the context of colocalized multiparametric MR imaging and histopathologic assessment of normal and abnormal regions by using whole-exome sequencing.

Advances in Knowledge

- Mutations in cancer-related genes were identified in normal and histopathologic analysis–proven high-grade regions of prostate glands in patients with histopathologic analysis–confirmed prostate adenocarcinoma, with no statistically significant difference (P = .30) in the number of cancer-related gene mutations in the regions found via histologic analysis to be normal or abnormal.
- Principal component analysis of DNA mutation profiles successfully classified 22 of 23 tissue samples from normal and high-grade prostate regions in terms of the individuals that the samples came from and Gleason score.

Implication for Patient Care

- Assessment of DNA mutations in prostate gland microenvironments in regions proven via histologic analysis to be normal and abnormal support the hypothesis that tumorigenesis in the prostate is not a discrete event, but rather part of a continuum in which unifocal versus multifocal disease is potentially within the same spectrum.

Materials and Methods

Patients and Materials

This was a Health Insurance Portability and Accountability Act–compliant, institutional review board–approved study that involved tissue and multiparametric prostate MR examinations in six retrospectively identified patients with a diagnosis of prostate adenocarcinoma and Gleason scores greater than or equal to 7 (3+4) between July 2009 and October 2011. Selection criteria was on the basis of acquisition of preoperative diagnostic multiparametric MR examinations in addition to paraffin-embedded whole mounts of the resected prostates with adequate tissue for DNA extraction from areas determined via histopathologic analysis to be normal and abnormal, and normal but with appearance at MR imaging that was mildly or moderately suspicious for cancer. Initially, 104 patients were identified with preoperative multiparametric MR imaging who were then cross-matched with available tissue whole mounts at the Translational Pathology Core Laboratory at University of California, Los Angeles, with confirmed adenocarcinoma and at least one other region at MR imaging noted to be abnormal, reducing the list to 14 patients of which one was Gleason score 3+3. The remaining 13 patients were evaluated

Published online before print
10.1148/radiol.2017162827 **Content codes:** GU MR

Radiology 2017; 000:1–11

Abbreviation:
PI-RADS = Prostate Imaging Reporting and Data System

Author contributions:
Guarantor of integrity of entire study, M.D.K.; study concepts/study design or data acquisition or data analysis/interpretation, all authors; manuscript drafting or manuscript revision for important intellectual content, all authors; approval of final version of submitted manuscript, all authors; agrees to ensure any questions related to the work are appropriately resolved, all authors; literature research, N.J., J.H., M.D.K.; clinical studies, all authors; experimental studies, N.J., M.D.K.; statistical analysis, N.J., M.D.K.; and manuscript editing, all authors

Conflicts of interest are listed at the end of this article.

Table 1

MR Imaging Pulse Sequence Characteristics

Pulse Sequence	Orientation	TR/TE (msec)	FOV (mm)	Matrix	Thickness (mm)
3D TSE T2 (SPACE)	Axial	3800/101	140	256 × 256	1.5
2D TSE T2	Axial, Coronal	3800/101	200	320 × 320	3.6
Echo planar DWI	Axial	3900/60	210 × 260	130 × 160	3.6
Dynamic contrast enhancement (TWIST)	Axial	3.9/1.4	260	160 × 160	3.6
MR signal intensity	Axial	1000/120	80	12 × 12	15

Note.—The parameters were as follows: three-dimensional turbo spin-echo T2-weighted imaging (SPACE), echo train length of 13; two-dimensional turbo spin-echo T2-weighted imaging, echo train length of 13–25; echo-planar diffusion-weighted imaging, *b* values of 0, 100, 400, and 800 sec/mm^2; dynamic contrast–enhanced (time-resolved angiography with interleaved stochastic trajectories) imaging, 12° flip angle, 4.75 seconds per acquisition over 5 minutes; MR signal intensity, 1300 Hz, six averages, 256 spectral points. 2D = two dimensional, 3D = three dimensional, DWI = diffusion-weighted imaging, FOV = field of view, SPACE = sampling perfection with application optimized contrasts using different flip-angle evolution, TE = echo time, TR = repetition time, TSE = turbo spin echo, TWIST = time-resolved angiography with interleaved stochastic trajectories.

on the basis of availability of adequate quantities of tissue for whole-exome sequencing, which resulted in the six glands ultimately analyzed in this study.

Preoperative 3-T pelvic multiparametric MR imaging (Siemens, Erlangen, Germany) with endorectal coils was performed on all patients. The examinations included T1-weighted imaging, T2-weighted turbo spin-echo imaging, diffusion-weighted imaging, T2 water and fat-saturated three-dimensional spectroscopic imaging, and intravenous contrast material–enhanced T1-weighted gradient-echo fat-saturated images before and after administration of gadolinium chelate (Table 1). Imaging examinations were reviewed by an abdominal and genitourinary radiologist (D.J.M., with 10 years of experience). Objective and subjective assessment of the glands was performed through standardized assessment of T2 signal, estimation of the average apparent diffusion coefficients, pharmacokinetic enhancement curve characteristics from dynamic contrast–enhanced images, and spectroscopic imaging (18), with prospective evaluation on a five-point ranked categorical scale as previously described by Le et al (19) and is the standard of care at our institution.

Each prostate gland was sectioned at 4–5 mm intervals. By using a whole-mount technique, tissue slices were then formalin fixed, paraffin embedded, and microtome cut (20,21). Gleason scoring was performed according to the 2005 International Society of Urological Pathology consensus recommendations (22).

Part of the motivation of this study was to characterize focal areas of the prostate, or microenvironments, that showed concordance between histopathologic analysis and multiparametric MR imaging in addition to characterizing regions that were normal by histopathologic appearance but demonstrated some imaging abnormalities that were not suspicious for cancer by Prostate Imaging Reporting and Data System (PI-RADS)–like criteria (23,24). For example, a focal nodule in the peripheral zone may exhibit decreased T2 signal intensity, an apparent diffusion coefficient of 1300 mm^2/sec, but no abnormal enhancement and normal spectroscopy; this would not warrant tissue sample by clinical standards, but would be included in the "mildly suspicious" category. Four different regions of interest were targeted within each gland from the whole-mount paraffin-embedded surgically resected prostates on the basis of the combination of pathologic and imaging criteria to construct the following imaging score matrix (Appendix E1 [online]): normal peripheral zone (normal by both histopathologic analysis and multiparametric MR imaging), mildly suspicious (normal by histopathologic analysis and PI-RADS score >1 to < 3), moderately suspicious (normal by histopathologic analysis and PI-RADS score ≥3 to <4), and abnormal (referred to as "path," based on histopathologic analysis, Gleason score of 3+4, and PI-RADS score of 4). Each gland was re-evaluated by a genitourinary pathologist (J.H., with >20 years of experience in genitourinary pathologic analysis) to confirm the initial diagnosis and to also identify appropriate regions to obtain tissue samples from (ie, one region within the high-grade area and three areas that were normal-appearing by histopathologic analysis but still within the peripheral zone of the gland).

Matching was performed during scheduled dedicated sessions where the pathologist, radiologist, and research staff would review the MR image and whole-mount histopathologic analysis to determine whether a finding at MR imaging constituted a match on the whole mount, as part of clinical quality assurance, with mismatches characterized as false-negative findings (ie, cancers that were not prospectively identified at MR imaging) and false-positive findings (ie, lesions on MR images that did not correspond to cancer). Therefore, the prospectively identified regions of interest on MR images with their corresponding categorical and quantitative assessments were correlated with cancerous (or benign) regions on the whole mount.

Isolated tissue samples were provided to Otogenetics (Otogenetics Corporation, Atlanta, Ga) for whole-exome DNA sequencing with Illumina HiSEquation 2000 sequencers (Illumina, San Diego, Calif) with paired-end reads of 90–100 nucleotides, greater than or equal to 50 times coverage. The "moderately suspicious" tissue sample from patient 3 was of insufficient quality to sequence, resulting in 23 samples with whole-exome sequencing in total from six patients. Intron and nonsynonymous mutations were excluded. Furthermore,

we only included mutations that were detected in at least two of the 23 independent samples. To identify mutations that were more likely to be related to the underlying malignancy within the tumors, we focused our analysis by using a list of curated genes in the literature that have been associated with cancer (25). The gene set of interest was reduced by finding the intersection with the Catalogue of Somatic Mutations in Cancer database (25). The mutation profiles were used to define mutation score matrices (Appendix E1 [online]).

Table 2

Summary of Patient Characteristics

Patient No.	Age (y)	PSA (ng/mL)	Gleason Score	Stage
1	70	7.1	4 + 5	T3a, NX, MX
2	70	0.8	4 + 5	T3a, N0, MX
3	68	6.1	3 + 4	T2c, N0, MX
4	68	6.1	4 + 5	T2c, N0, MX
5	74	18.9	3 + 4	T3a, N0, MX
6	66	9.5	3 + 4	T3a, N0, MX

Note.—There was no statistically significant difference between the ages of the patients. Elevated prostate-specific antigen results from screening examinations prompted referral for multiparametric MR imaging for all patients except patient 2, who was found to have a palpable nodule at physical examination and was referred for imaging evaluation despite a normal prostate-specific antigen. PSA = prostate-specific antigen.

Statistical Analysis

We performed the Kruskal-Wallis test to assess any statistically significant variations among the tissue sample physical locations, tissue classification, Gleason scores, chromosomal location, and mutation profiles. We performed two-way hierarchical clustering with complete linkage by using the Euclidean norm on the imaging score matrix and the mutation score matrix. A phylogenetic tree was constructed from the pairwise distances between the samples on a mutation-by-mutation basis. We calculated the cophenetic coefficient for the entire tree and performed principal component analysis of the signed binary mutation matrix. We analyzed the highest ranking principal components, which accounted for at least 50% of the variation across all of the samples. Assessment of the most significant genes contributing to the third principal component was assessed by selecting the genes with absolute value greater than 0.4. The Student *t* test was performed to assess any statistically significant age difference between the Gleason score subgroups. Pearson correlation coefficients were calculated between the ordinal imaging scores and the mutation (weighted and binary) matrices on a sample-by-sample basis. Multiple hypothesis correction was performed by using the Bonferroni method. Data processing, calculations, and figure generation were performed by using software (Python v2.7, Matlab 2015b, MathWorks, Natick, Mass; and R v3.1.1, R Project for Statistical Computing, *www.r-project.org*).

Please refer to the Appendix E1 (online) for additional details.

Results

Patients

Six patients with prostate adenocarcinoma were identified (three patients with Gleason score of 3+4; mean age, 68 years [age range, 66–74 years]; and three patients with Gleason score of 4+5; mean age, 68 years [age range, 68–70 years]). There was no statistically significant difference between the two groups on the basis of age (Student *t* test, $P > .999$) (Table 2).

Multiparametric MR Imaging

The whole-mount prostate specimens in conjunction with three-dimensional anatomic MR imaging enabled tissue samples to be analyzed from focal regions, or microenvironments, of the glands by using imaging, and it enabled histopathologic analysis–based characterization (Fig 1). Regions with combinations of T2 shortening, impaired diffusion, abnormal enhancement characteristics, and/or elevated choline were concordant with high-grade regions proven with histologic analysis (Fig 1; Tables E1, E2 [online]; Appendix E1 [online]), consistent with findings in the literature (4,26,27).

Unsupervised hierarchical clustering of multiparametric MR imaging features (T2 signal, apparent diffusion coefficient, contrast enhancement curve, and spectroscopy) across all samples and patients revealed clustering of samples according to normal and histopathologic groups (Fig 2). As expected, normal multiparametric MR imaging samples were in a subcluster and nodules suspicious for cancer (ie, high) were in a separate subcluster. The mild regions clustered with the normal regions of interest and the moderate regions clustered with the nodules suspicious for cancer. The separation of regions of interest that were normal and suspicious for cancer is consistent with observations in the literature and PI-RADS–based classification for radiology-pathologic (known as rad-path) correlations between multiparametric MR imaging and histologic analysis differentiating normal tissue from tumor.

Whole-Exome DNA Sequencing

Global assessment of single nucleotide variants revealed 94 166 cumulative variant calls across all samples (Fig 3). The majority of mutations were nonsynonymous mutations (97.2% [91 578 of 94 166]), with only 1.5% (1380 of 94 166) frameshift mutations and 1.3% (1199 of 94 166) stop-gain or stop-loss mutations identified. There was no evidence of bias or significant association between the different microenvironments and the chromosomal location of the mutations (Kruskal-Wallis test, $P = .268$) or with the different microenvironments and type of mutation (eg, frameshift, nonsynonymous, stop gain, stop loss)

Figure 1

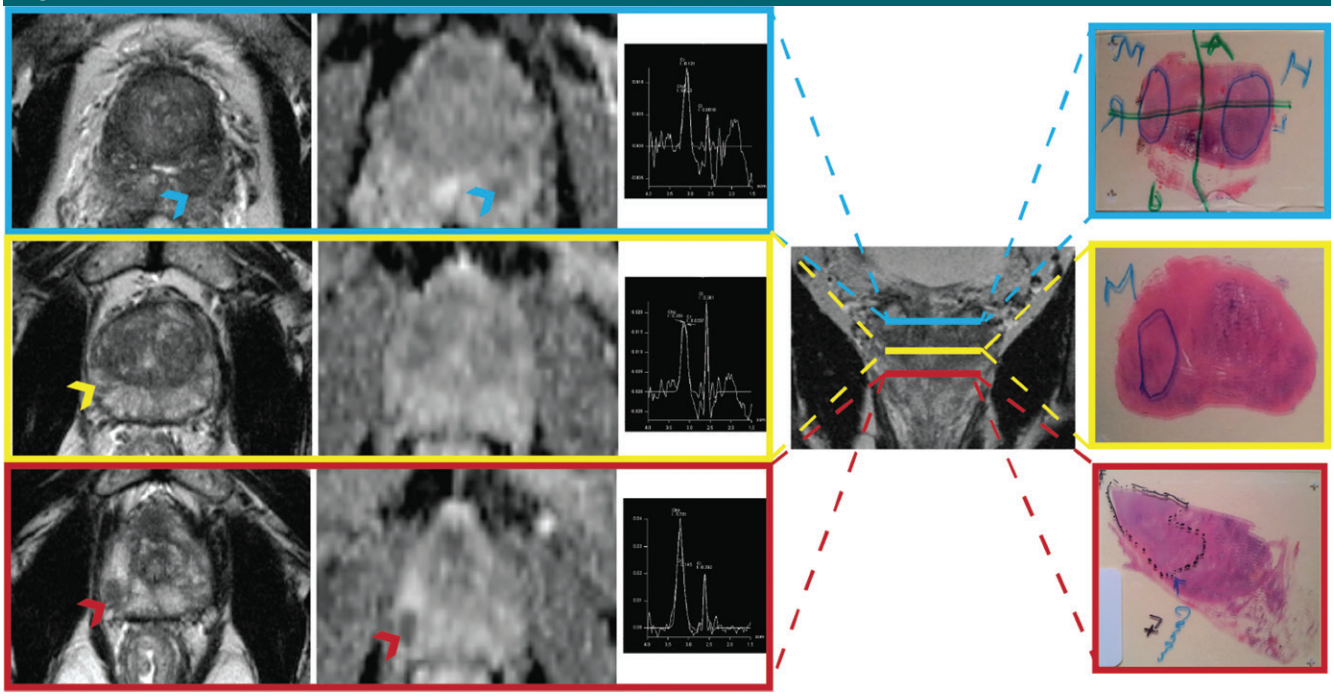

Figure 1: Mapping between three-dimensional prostate whole mounts and multiparametric MR imaging. Tissue sections from whole-mount slides correspond to different regions of interest: adenocarcinoma (Gleason score, ≥3+4) in red outline; moderately suspicious according to multiparametric MR imaging in blue outline; and mildly suspicious by multiparametric MR imaging in yellow outline. The nodule of interest (arrowheads) is shown in each of the fields of view, which are, from left to right: axial T2-weighted image, apparent diffusion coefficient map, spectroscopy profile, and coronal T2-weighted images (which map to the corresponding axial multiparametric MR imaging images and histologic sections), and annotated whole-mount section. The red outlined images highlight a cancer nodule in the right apical posterior peripheral zone: adenocarcinoma with radiologic and pathologic-analysis concordance with abnormal T2 signal, positive diffusion restriction with apparent diffusion coefficient of 1015 mm^2/sec, and abnormal spectroscopy (ie, reversal of choline and creatine-to-citrate ratio) that was sectioned and whole-exome sequenced according to the dotted black line in the tissue section (right-hand side). The blue outlined images depict a lesion moderately suspicious for cancer (that was normal according to histopathologic analysis) but with abnormal hypointense T2 signal, apparent diffusion coefficient of 1347 mm^2/sec reflecting some restricted diffusion, and normal spectroscopy. The yellow outlined images highlight a histologically normal nodule with abnormal T2 signal hypointensity but no evidence or diffusion or spectroscopic abnormalities.

Figure 2

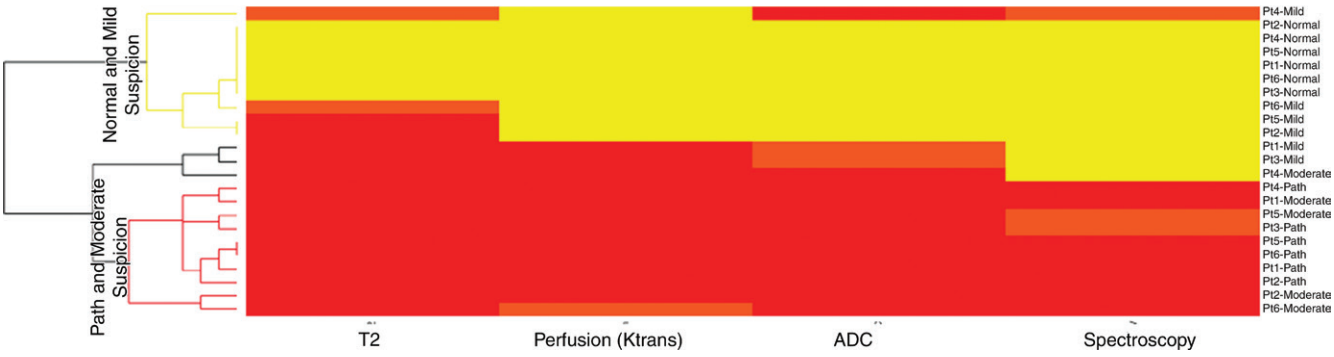

Figure 2: One-way hierarchical clustering of multiparametric features across 23 regions of interest in six patients show radiologic and pathologic (*path*) concordance. Red colored blocks reflect abnormal feature values (eg, decreased T2 signal intensity, decreased diffusion, wash-in and/or wash-out enhancement characteristics, and abnormal spectroscopy) and yellow blocks reflect normal parameter measurements. The two principle branches of the dendrogram across the x-axis segregate the samples into normal and abnormal according to histopathologic analysis, with multiparametric MR imaging classified samples mildly and moderately suspicious for cancer intermixed among the two principle groups. *Ktrans* = volume transfer constant.

Figure 3

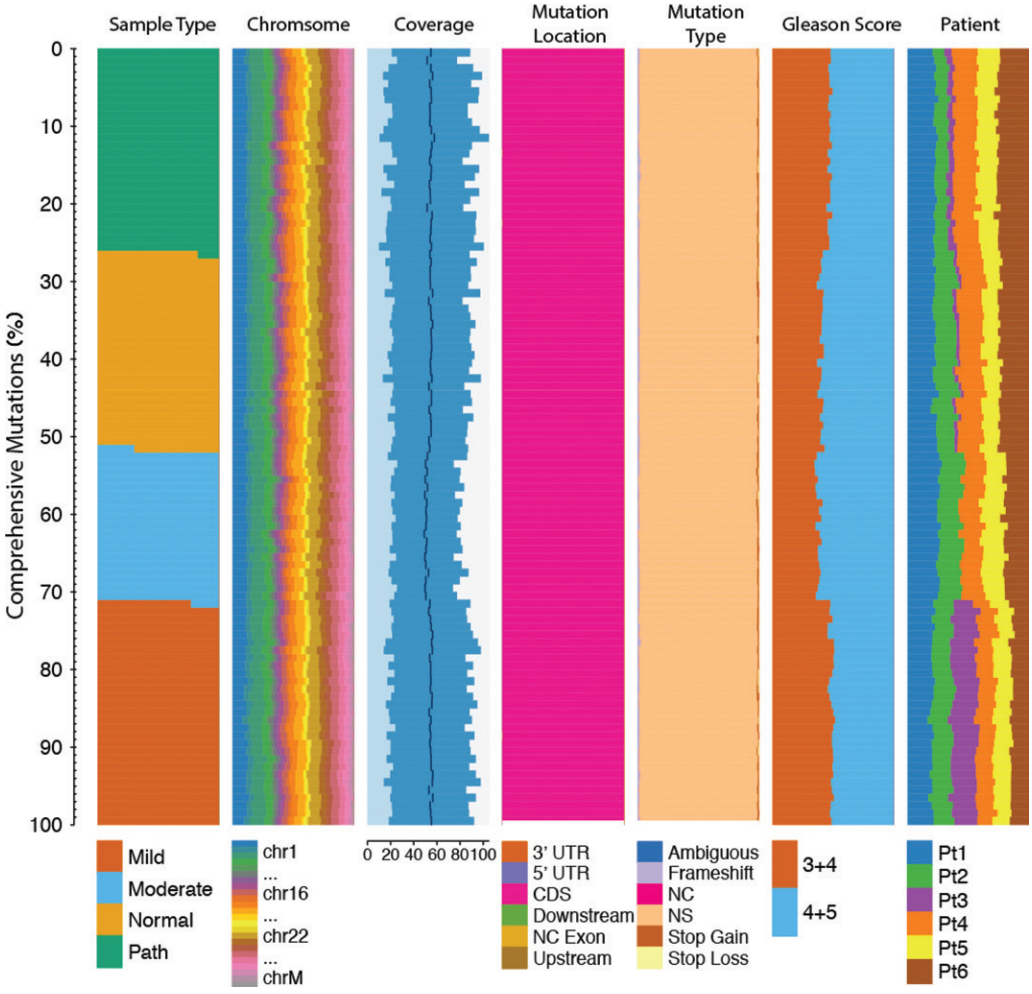

Figure 3: Overview of cumulative nonintronic, annotated mutations across all 23 samples. The majority of mutations were nonsynonymous (*NS*) with less than 3% and composed of frameshift, stop-gain, or stop-loss mutations. Each subpanel from left to right summarizes the 94 166 mutations, starting with the first mutation in the upper left and the last mutation in the lower right of each vertical panel. The subpanels consist of 94 166 small rectangular boxes that correspond to individual mutations, the coordinates of each subrectangle within each column correspond to the same mutation across all panels (except for the coverage panel, which summarizes the average across each corresponding row). *NC* = noncoding, *UTR* = untranslated region. Visually there was no evidence of significant biases between the different microenvironments and the location or types of mutations. There is the suggestion of significant variation in mutation coverage for patient 3, which was confirmed statistically (Kruskal-Wallis test, $P < 2e\text{-}16$).

identified (Kruskal-Wallis test, $P = .224$). However, there was significant variation observed in mutation coverage among the different tissue samples (Kruskal-Wallis test, $P < 2e\text{-}16$); this was primarily attributable to samples from patient 3 (high-grade tissue sample and normal (histopathologic analysis and multiparametric MR imaging) sample (Figs E1, E2 [online]).

Next, we focused the analysis on the subset of curated cancer-associated genes from the Catalogue of Somatic Mutations in Cancer database; removal of noncancer-associated mutations was accompanied by a decrease in variation between individual tissue samples, which suggested that the vast majority of variant calls, which were filtered out, were likely passenger mutations (Figs E3, E4 [online]; Table E3 [online]). There was no significant variation in cancer-associated variants (mutations) among the four different groups (histopathologic analysis–confirmed normal, 34 mutations per sample ± 19 [standard deviation]; multiparametric MR imaging–confirmed mild suspicion, 37 mutations per sample ± 21; multiparametric MR

Figure 4

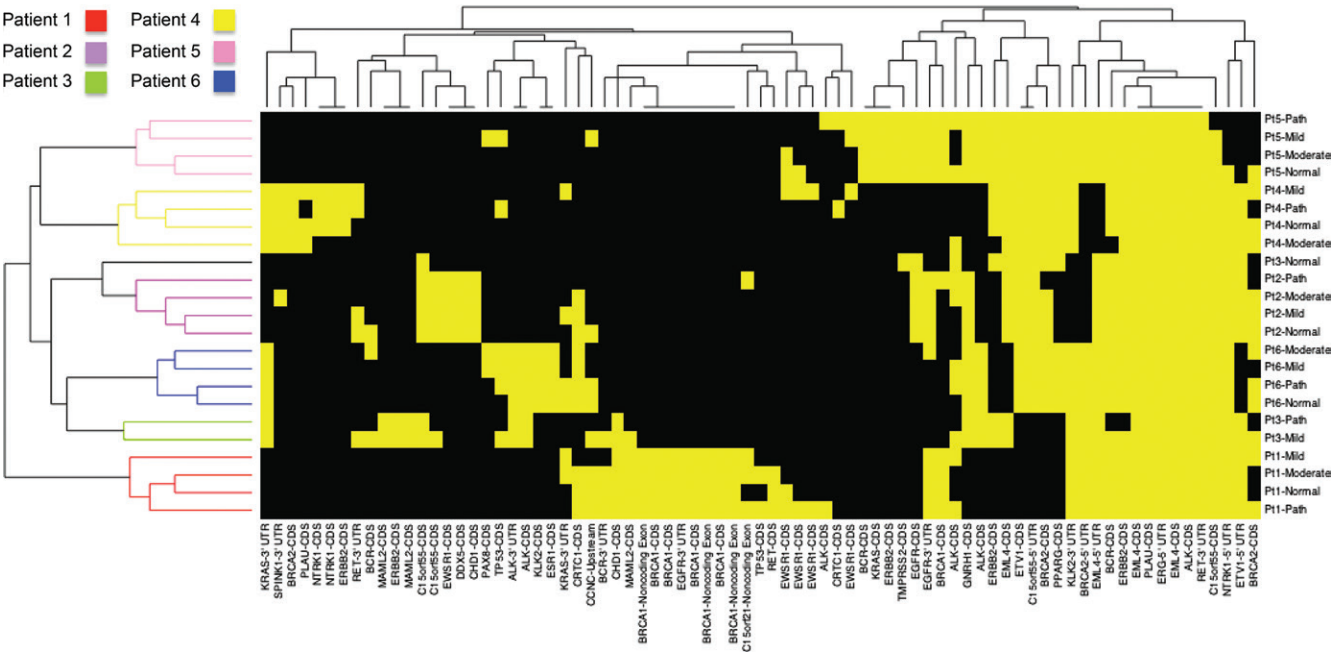

Figure 4: Two-dimensional hierarchical clustering of data of mutations versus the colocalized genomic-sampled regions show clustered subgroups that correspond to individual patients. Row dendrogram (left side) corresponds to clustering of the colocalized genomic-sampled regions and are colored coded by patient and similarly labeled by patient number, tissue location, and classification (ie, normal, mild, moderate, and path) on the right. Samples clustered most strongly by groups of individual patients, as color coding of the patient specific subbranches reflect. Column dendrogram (top) reveals clustering of filtered and annotated mutations. Yellow reflects the presence of a mutation and black reflects an absence. Additional detailed annotations of the mutations are provided in Tables E4 and E5 (online).

imaging–confirmed intermediate suspicion, 31 mutations per sample ± 15; and high grade, 33 mutations per sample ± 18; Kruskal-Wallis test, $P = .30$). Interestingly, mutations in cancer-associated genes were observed in all of the regions sampled (including regions in which the histologic structure appeared normal [referred to here as histologically normal]) across all of the patients for the cumulative set of mutations and the filtered cancer gene mutations.

We subsequently identified 77 unique mutations mapping to 29 genes across 16 chromosomes in the 23 tissue samples from the total cohort (Table E4 [online]). The majority of these mutations (53 of 77) were nonsynonymous coding mutations across 26 different genes. Additionally, a frameshift mutation in BCR was detected in samples from patients 2, 3, and 6. A frameshift mutation in TP53 was detected in the high-grade samples and histologically normal microenvironment samples that were also moderately suspicious for cancer from patient 1. There were three-stop gain mutations in EWSR1 (patients 1, 4, and 5). Hierarchical clustering of the mutations across all 23 samples was then performed to assess any underlying association or natural grouping of these mutations across the different tissue samples (Fig 4). Interestingly, the clustered subgroups corresponded to the individual patients. Six mutations across five genes (*ALK*, *ERG*, *EML4*, *PLAU*, and *RET*) were detected in all of the samples, with subgroups of mutations driving clusters specific to each individual (Fig 4; Tables E4, E5 [online]).

Radiogenomic Assessment

Phylogenetic analysis of the complete set of samples revealed a branching pattern that grouped together by patient at the most distal end (ie, leafs), although grouping according to groups of mutations was noted more proximally (Fig 5). The cophenetic correlation across the entire tree was 0.91. The branching pattern of the tree revealed the highest concordance among independent tissue samples from different regions of the prostate that were acquired from the same patient, which provided a degree of validation of the mutations. Tissues that were normal and proved to be abnormal by histologic analysis (and imaging) were not as dissimilar as might have been anticipated (normal and high-grade samples were the last to split into separate branches in four of the six patients). The mutation profiles for patients 1 and 3 branch early in the tree and are more distinct than that of the other patients.

To further delineate grouping of the samples on the basis of mutation characteristics, principal component analysis was performed (Fig 6). The first three principal components accounted for 65% of the variation of

Figure 5

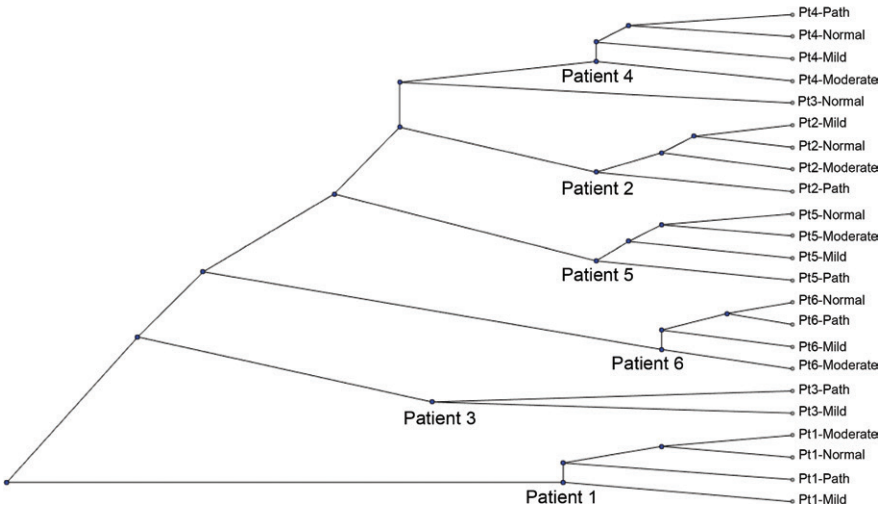

Figure 5: Phylogenetic tree generated from the mutations across all patient samples show branching and grouping according to cancer-related mutations shared within patients (vs mutations in tissue samples shown via histologic analysis to be similar). The root of the phylogenetic tree (most commonly shared mutations appears) are on the far left and the leaves of the tree (most distinct or unique mutations) are on the far right. Reading the plot from left to right, the most similar tissue samples on the basis of mutations in genes related to cancer will branch later (more toward the right). There is a branching structure of the mutations, grouping according to the individual prostate glands (including normal and histologically abnormal tissue), and separation between histologically normal versus high-grade specimens in the most terminal branches, which reflects greater similarity within each gland rather than between different glands, regardless of histologic analysis (ie, tissue samples that are histologically normal as well as abnormal from the same patient have more in common than Gleason 3+4 and 4+5 nodules from different patients). Relatively early branching of patients 1 and 3 suggest that their mutation profiles are more distinct than that of the other patients.

the mutations across all tissue samples. Classification of the samples by patient and Gleason score by using the first three principal components resulted in simultaneous classification of individual patients and Gleason scores of 3+4 versus 4+5 lesions for 22 of the 23 samples. The second and third principal components only accounted for 24.9% of the mutational variance across all samples; however, by using only these two components, 20 of 23 of the individual patient samples with Gleason scores of 3+4 versus 4+5 were successfully classified (Fig E5 [online]). This separation is driven primarily by the third principal component; the genes with the largest weightings included *KLK2* (rs198977), *KRAS* (rs712), *SPINK1* (rs11319), *BRCA1* (rs1799949), and *BCR*.

No statistically significant linear correlation was identified between individual mutations and functional MR imaging parameters, although it was noted that before multiple hypotheses corrections there was a significant correlation between two genes with contrast-agent enhancement (*BRCA2*, rs144848, $P = .045$; and *ALK*, rs1881421, $P = .046$). No significant correlations were identified between the composite PI-RADS scores and individual mutations.

Discussion

This study provides a detailed spatial radiogenomic characterization of prostate glands in six patients with confirmed high-grade tumors through evaluation of the histologically normal and abnormal microenvironments of the glands by using multiparametric MR imaging, histopathologic assessment, and whole-exome sequencing. The investigation was enabled by the technologic advancements that have been made in multiple fields, including whole-mount tissue preservation, multiparametric MR imaging capabilities, and next-generation sequencing technologies. This integrative study revealed the presence of cancer-related mutations within multiple microenvironments of prostate glands, including histologically normal and abnormal (ie, high-grade) regions; thus, exome sequencing can potentially provide a complementary role to multiparametric MR imaging and histopathology in characterizing prostate adenocarcinoma.

We observed that the background mutational spectrum in the prostate gland is greater than expected and, not surprisingly, that abnormalities found via histopathologic analysis may not be the earliest harbingers of disease. This observation supports a hypothesis that tumorigenesis in the prostate is not a discrete event, but rather part of a continuum in which unifocal versus multifocal disease are potentially within the same spectrum, in which the latter declares itself because of either diagnosis at a later stage of the disease process or a propensity for forming multiple nodules earlier because of underlying biologic variation. In light of the evidence of so-called field effects in the prostate gland and further evidence that revealed shared mutational variation in histologically normal and abnormal regions of prostates with foci of adenocarcinoma (28,29), multifocal disease may be seen as more of a distal part of the spectrum of prostate cancer from the perspective of mutational burden (20).

There is literature (30–34) that supports evidence of abnormal mutations in normal-appearing tissues in other organs including skin, lung, and ovaries. Regions that harbor abnormal mutations may presage organizational changes on the molecular level that are not yet discernable via conventional light microscopy. Changes in multiparametric MR imaging characteristics (ie, diffusion, T2-weighted signal, and tissue perfusion) reflect alterations in tissue organization, structure, and

Figure 6

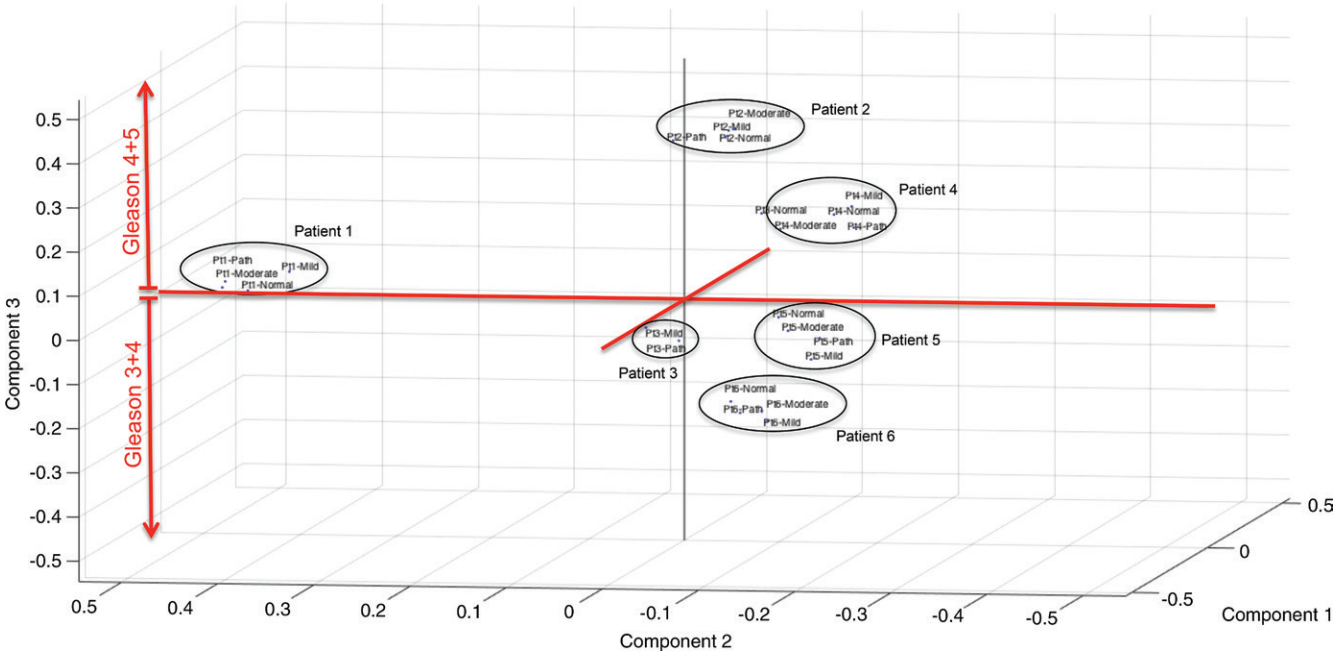

Figure 6: Principal component analysis of mutations across all 23 prostate tissue samples enabled stratification according to Gleason score and individual patient identification. The first three principal components of the individual genomic sampled regions clearly group by individual patients and are also able to classify different histopathologic grades of tumors according to the mutations. The third principle component separates the patients into higher (Gleason 4+5) and lower grade (Gleason 3+4) groups (demarcated by the intersecting plane composed of the first and second principal component axes in red), which shows histopathologic and mutation profile coherence.

vascularity; however, identification of associated inconsequential genomic variation versus malignancy-associated mutations remains a challenge. For the prostate, this raises important questions to be addressed in future work, including the significance of such mutations and determining the likelihood of whether such mutations will lead to a malignant nodule, and if so, which other associated factors could drive (or avoid) such transformations.

This study had limitations. First, the sample size of the study was limited; this was primarily the result of limited availability of high-quality tissue in addition to cost considerations. Whereas the principle observation suggestive of field effect for prostate cancer is compelling and supported by other observations in the literature (28,29), identification of diagnostic mutation profiles needs to be performed with larger sample cohorts in studies designed for that purpose. Second, this was a retrospective study; this was a requisite by design and the underlying evaluated hypothesis, which required confirmed diagnoses of prostate adenocarcinoma. Although Gleason score could be assessed for the different samples, clinical outcomes or other phenotypic measures could not be performed; this is because of the indolent nature of the disease. Additional measurements would have been beneficial for confirming the significance of the measured mutations; however, limitations in tissue availability and cost curbed the ability to perform additional measurements. This unfortunately also limited the ability to assess the degree of causality of the mutations. Similarly, for normalization it would have been preferable to have obtained whole blood at the time of surgery (also a limitation of the retrospective nature of the study). However, by focusing on genes with associated cancer mutations (Catalogue of Somatic Mutations in Cancer database) and further focusing only on mutations that were identified in at least two or more different tissue samples, we were able to significantly increase the specificity of the targeted mutations.

In spite of these limitations, the assessment of the imaging, histopathologic analysis, and exomes across multiple microenvironments of the prostate in patients with prostate adenocarcinoma enabled characterization of the mutational background of the gland. Although we did not identify any significant correlations between the mutation profiles and multiparametric MR imaging measures, this may have been a limitation of the sample size because recent studies (35,36) investigating imaging correlates of multiparametric MR imaging and gene expression in prostate cancer show some promise for possible association maps to be constructed. Additionally, although detailed review by a genitourinary pathologist and genitourinary radiologist to

ensure concordance of MR imaging and histologic specimens supported spatial concordance of the multiparametric MR imaging description and sequenced tissue, the development of objective, electronic registration of whole mounts with MR imaging (37–39) could assist in colocalizing lesions with greater accuracy, accounting for differences in nonconcordance of the axial axis in the MR versus the whole-mount sections (ie, obliquities between multiparametric MR imaging axial and whole-mount specimen slices).

Rad-path correlation is established with PI-RADS; however, with additional dimensions of measurement, including next-generation sequencing, it may be possible to move beyond current classification, toward molecular-Rad-Path correlations and so-called Rad-Path 2.0 (40). These results suggest that tumorigenesis in the prostate is part of a continuum in which abnormal mutations and imaging features that are moderately suspicious for cancer may predate histopathologic analysis–proven abnormalities that become apparent at a later time. Although there is evidence to support the use of targeted tissue biopsies when relying on histologic analysis alone (41), findings in this study and the mutational landscape, with a background of abnormal mutations in normal and abnormal (by histopathologic analysis) regions of the prostate, suggest that random, nontargeted biopsies may be useful in genomic-driven treatment decision making, although larger cohort studies are required to address this more definitively.

This work takes a further step in assessing the imaging and genomic features in prostate glands with adenocarcinoma, with the purpose of elucidating both the so-called natural course of the disease and the ways in which diagnostic tools can contribute to the detection of this disease. Multiparametric MR imaging and DNA mutation measurements are found to be complementary, in which the multiparametric MR imaging correlates strongly with histopathologic analysis, and DNA mutations from microenvironments proven via histologic analysis to be normal may intimate high–Gleason score nodules elsewhere in the gland, potentially reflecting latent, smoldering disease. Although these results are encouraging, additional larger studies are needed to further evaluate the potential significance of these observations and to further evaluate correlates between sequence variation and imaging characteristics.

Acknowledgments: The authors gratefully acknowledge generous support from the Prostate Cancer Foundation and the UCLA Prostate Cancer National Cancer Institute Specialized Program of Research Excellence (Principal Investigator, Reiter).

Disclosures of Conflicts of Interest: N.J. disclosed no relevant relationships. **D.J.M.** Activities related to the present article: disclosed no relevant relationships. Activities not related to the present article: author disclosed personal fees from Blue Earth Diagnostics. Other relationships: disclosed no relevant relationships. **S.R.** disclosed no relevant relationships. **J.H.** disclosed no relevant relationships. **R.E.R.** disclosed no relevant relationships. **MD.K.** disclosed no relevant relationships.

References

1. Siegel RL, Miller KD, Jemal A. Cancer statistics, 2017. CA Cancer J Clin 2017;67(1):7–30.
2. Smith CV, Bauer JJ, Connelly RR, et al. Prostate cancer in men age 50 years or younger: a review of the Department of Defense Center for Prostate Disease Research multicenter prostate cancer database. J Urol 2000;164(6):1964–1967.
3. Brassell SA, Rice KR, Parker PM, et al. Prostate cancer in men 70 years old or older, indolent or aggressive: clinicopathological analysis and outcomes. J Urol 2011;185(1):132–137.
4. Portalez D, Mozer P, Cornud F, et al. Validation of the European Society of Urogenital Radiology scoring system for prostate cancer diagnosis on multiparametric magnetic resonance imaging in a cohort of repeat biopsy patients. Eur Urol 2012;62(6):986–996.
5. Rigler LG. The natural history of untreated lung cancer. Ann N Y Acad Sci 1964;114(2):755–766.
6. Nowell PC. The clonal evolution of tumor cell populations. Science 1976;194(4260):23–28.
7. Hanahan D, Weinberg RA. Hallmarks of cancer: the next generation. Cell 2011;144(5):646–674.
8. Almendro V, Marusyk A, Polyak K. Cellular heterogeneity and molecular evolution in cancer. Annu Rev Pathol 2013;8:277–302.
9. Gerlinger M, Rowan AJ, Horswell S, et al. Intratumor heterogeneity and branched evolution revealed by multiregion sequencing. N Engl J Med 2012;366(10):883–892.
10. Yamamoto S, Korn RL, Oklu R, et al. ALK molecular phenotype in non-small cell lung cancer: CT radiogenomic characterization. Radiology 2014;272(2):568–576.
11. Yamamoto S, Han W, Kim Y, et al. Breast cancer: radiogenomic biomarker reveals associations among dynamic contrast-enhanced MR imaging, long noncoding RNA, and metastasis. Radiology 2015;275(2):384–392.
12. Segal E, Sirlin CB, Ooi C, et al. Decoding global gene expression programs in liver cancer by noninvasive imaging. Nat Biotechnol 2007;25(6):675–680.
13. Kickingereder P, Bonekamp D, Nowosielski M, et al. Radiogenomics of glioblastoma: machine learning-based classification of molecular characteristics by using multiparametric and multiregional MR imaging features. Radiology 2016;281(3):907–918.
14. Jamshidi N, Jonasch E, Zapala M, et al. The radiogenomic risk score stratifies outcomes in a renal cell cancer phase 2 clinical trial. Eur Radiol 2016;26(8):2798–2807.
15. Jamshidi N, Jonasch E, Zapala M, et al. The Radiogenomic Risk Score: construction of a prognostic quantitative, noninvasive image-based molecular assay for renal cell carcinoma. Radiology 2015;277(1):114–123.
16. Aerts HJ, Velazquez ER, Leijenaar RT, et al. Decoding tumour phenotype by noninvasive imaging using a quantitative radiomics approach. Nat Commun 2014;5:4006.
17. Gevaert O, Xu J, Hoang CD, et al. Non-small cell lung cancer: identifying prognostic imaging biomarkers by leveraging public gene expression microarray data--methods and preliminary results. Radiology 2012;264(2):387–396.
18. Sonn GA, Chang E, Natarajan S, et al. Value of targeted prostate biopsy using magnetic resonance-ultrasound fusion in men with prior negative biopsy and elevated prostate-specific antigen. Eur Urol 2014;65(4):809–815.
19. Le JD, Stephenson S, Brugger M, et al. Magnetic resonance imaging-ultrasound fusion biopsy for prediction of final prostate pathology. J Urol. 2014;192(5):1367–73.
20. Le JD, Tan N, Shkolyar E, et al. Multifocality and prostate cancer detection by multiparametric magnetic resonance imaging:

correlation with whole-mount histopathology. Eur Urol 2015;67(3):569–576.

21. Tan N, Margolis DJ, Lu DY, et al. Characteristics of detected and missed prostate cancer foci on 3-T multiparametric MRI using an endorectal coil correlated with whole-mount thin-section histopathology. AJR Am J Roentgenol 2015;205(1):W87–W92.

22. Epstein JI, Allsbrook WC Jr, Amin MB, Egevad LL; ISUP Grading Committee. The 2005 International Society of Urological Pathology (ISUP) Consensus Conference on Gleason Grading of Prostatic Carcinoma. Am J Surg Pathol 2005;29(9):1228–1242.

23. Weinreb JC, Barentsz JO, Choyke PL, et al. PI-RADS Prostate Imaging - Reporting and Data System: 2015, Version 2. Eur Urol 2016;69(1):16–40.

24. Rosenkrantz AB, Ginocchio LA, Cornfeld D, et al. Interobserver reproducibility of the PI-RADS Version 2 lexicon: a multicenter study of six experienced prostate radiologists. Radiology 2016;280(3):793–804.

25. Forbes SA, Beare D, Gunasekaran P, et al. COSMIC: exploring the world's knowledge of somatic mutations in human cancer. Nucleic Acids Res 2015;43(Database issue):D805–D811.

26. Hamoen EH, de Rooij M, Witjes JA, Barentsz JO, Rovers MM. Use of the Prostate Imaging Reporting and Data System (PI-RADS) for prostate cancer detection with multiparametric magnetic resonance imaging: a diagnostic meta-analysis. Eur Urol 2015;67(6):1112–1121.

27. Schimmöller L, Quentin M, Arsov C, et al. MR-sequences for prostate cancer diagnostics: validation based on the PI-RADS scoring system and targeted MR-guided in-bore biopsy. Eur Radiol 2014;24(10):2582–2589.

28. Cooper CS, Eeles R, Wedge DC, et al. Analysis of the genetic phylogeny of multifocal prostate cancer identifies multiple independent clonal expansions in neoplastic and morphologically normal prostate tissue. Nat Genet 2015;47(4):367–372.

29. Risk MC, Knudsen BS, Coleman I, et al. Differential gene expression in benign prostate epithelium of men with and without prostate cancer: evidence for a prostate cancer field effect. Clin Cancer Res 2010;16(22):5414–5423.

30. Vos S, Vesuna F, Raman V, van Diest PJ, van der Groep P. miRNA expression patterns in normal breast tissue and invasive breast cancers of BRCA1 and BRCA2 germ-line mutation carriers. Oncotarget 2015;6(31):32115–32137.

31. Martincorena I, Roshan A, Gerstung M, et al. Tumor evolution. High burden and pervasive positive selection of somatic mutations in normal human skin. Science 2015;348(6237):880–886.

32. Krimmel JD, Schmitt MW, Harrell MI, et al. Ultra-deep sequencing detects ovarian cancer cells in peritoneal fluid and reveals somatic TP53 mutations in noncancerous tissues. Proc Natl Acad Sci U S A 2016;113(21):6005–6010.

33. Gao W, Mady HH, Melhem MF, Keohavong P. Analysis of p53 mutations in histologically normal lung tissues and lung tumors from non-small cell lung cancer patients. Mol Carcinog 2009;48(7):633–641.

34. Aghili L, Foo J, DeGregori J, De S. Patterns of somatically acquired amplifications and deletions in apparently normal tissues of ovarian cancer patients. Cell Reports 2014;7(4):1310–1319.

35. Stoyanova R, Pollack A, Takhar M, et al. Association of multiparametric MRI quantitative imaging features with prostate cancer gene expression in MRI-targeted prostate biopsies. Oncotarget 2016;7(33):53362–53376.

36. McCann SM, Jiang Y, Fan X, et al. Quantitative multiparametric MRI features and PTEN expression of peripheral zone prostate cancer: a pilot study. AJR Am J Roentgenol 2016;206(3):559–565.

37. Kalavagunta C, Zhou X, Schmechel SC, Metzger GJ. Registration of in vivo prostate MRI and pseudo-whole mount histology using Local Affine Transformations guided by Internal Structures (LATIS). J Magn Reson Imaging 2015;41(4):1104–1114.

38. Gibson E, Crukley C, Gaed M, et al. Registration of prostate histology images to ex vivo MR images via strand-shaped fiducials. J Magn Reson Imaging 2012;36(6):1402–1412.

39. Commandeur F, Acosta O, Simon A, et al. Prostate whole-mount histology reconstruction and registration to MRI for correlating in-vivo observations with biological findings. Conference proceedings: Annual International Conference of the IEEE Engineering in Medicine and Biology Society IEEE Engineering in Medicine and Biology Society Annual Conference, 2015; 2399–2402.

40. Kuo MD, Yamamoto S. Next generation radiologic-pathologic correlation in oncology: Rad-Path 2.0. AJR Am J Roentgenol 2011;197(4):990–997.

41. Sonn GA, Natarajan S, Margolis DJ, et al. Targeted biopsy in the detection of prostate cancer using an office based magnetic resonance ultrasound fusion device. J Urol 2013;189(1):86–91.